PHILOSOPHICAL TRANSACTIONS A

rsta.royalsocietypublishing.org

Research

Article submitted to journal

Subject Areas:

xxxxx, xxxxx, xxxx

Keywords:

xxxx, xxxx, xxxx

Author for correspondence:

B. Ganapathisubramani

e-mail: G.Bharath@soton.ac.uk

Wind resource assessment in heterogeneous terrain

C. Vanderwel[1], M. Placidi[2], and B. Ganapathisubramani[1]

[1]University of Southampton, Southampton, UK

[2]City, University of London, UK

High-resolution Particle Image Velocimetry data obtained in rough-wall boundary layer experiments are re-analysed to examine the influence of surface roughness heterogeneities on wind resource. Two different types of heterogeneities are examined: 1) surfaces with repeating roughness units of the order of the boundary layer thickness [1] and 2) surfaces with streamwise-aligned elevated strips that mimic adjacent hills & valleys [2]. For the first case, the data shows that the power extraction potential is highly dependent on the surface morphology with a variation of up to 20% in the available wind resource across the different surfaces examined. A strong correlation is shown to exist between the frontal and plan solidities of the rough surfaces and the equivalent wind speed, and hence the wind resource potential. These differences are also found in profiles of $\overline{U^2}$ and $\overline{U^3}$ (wher U is the streamwise velocity), which act as proxies for thrust and power output. For the second case, the secondary flows that cause low- and high-momentum pathways when the spacing between adjacent hills is beyond a critical value, result in significant variations in wind resource availability. Contour maps of $\overline{U^2}$ and $\overline{U^3}$ show a large difference in thrust and power potential (over 50%) between hills and valleys (at a fixed vertical height). These variations do not seem to be present when adjacent hills are close to each other (i.e. when the spacing is much less than boundary layer thickness). The variance in thrust and power also appears to be significant in the presence of secondary flows. Finally, there are substantial differences in the dispersive and turbulent stresses across the terrain, which could lead to variable fatigue life depending on the placement of the turbines within such heterogeneous terrain. Overall, these results indicate the importance of accounting for heterogeneous terrain when siting individual turbines and wind-farms.

THE ROYAL SOCIETY PUBLISHING

1. Introduction

Surface roughness is found in abundance in natural environments and plays an important role in a variety of practical and engineering applications. Specifically, regularly distributed discrete roughness plays an important role in diverse energy and civil engineering applications, such as, pollutant dispersion modelling [3], wind-farms [4] and wind loading calculations [5]. Nevertheless, to date, the effect of surface morphology remains only partially understood and a number of fundamental questions remain unanswered. For example, it is still unclear which and how many parameters are necessary to characterise a rough-wall or to what extent the turbulence above the rough surface is effected by the wall morphology. This is especially true for heterogeneous surfaces where the spatial scales of the surface morphology are comparable to the integral scales of the flow within the boundary layer. This could have major implications on the kinetic energy available for extraction by a wind-farm that is located in a heterogeneous terrain.

It is necessary to understand the role of surface topography on determining the potential of wind-power resources, especially in complex terrain such as urban environments, hills/valleys, different croplands, etc. Fortunately, there are well-established methods for the determination and prediction of mean velocities over a homogeneous rough surface. Most of these methods have originated in studies that examined the influence of the land surface on the atmospheric flow. Specifically, the mean velocity over a rough surface can be represented using a logarithmic profile as

$$U = \frac{U_\tau}{\kappa} \ln\left(\frac{y-d}{y_0}\right), \tag{1.1}$$

where U is the mean streamwise velocity at height y above the ground, U_τ is the skin-friction velocity and κ is the von Kármán constant. The surface characteristics are represented by y_0, known as the aerodynamic roughness length, which essentially captures the momentum deficit incurred by the rough topography, and by d, known as the zero-plane displacement, which is often interpreted as the vertical location where the integrated drag force of the surface would act [6]. Large roughness features such as buildings, tall trees, wind turbines, etc. affect the wind profile over a large vertical extent, and therefore have larger roughness lengths than smaller roughness elements. Similarly, different roughness features result in varying values of d. The spatial configuration of the elements also influences the roughness length and zero-plane displacement. A dense, regular arrangement of roughness would affect the flow differently than sparse, irregular roughness distribution and generally cause variations in both y_0 and d.

Recent studies have examined the wind resource potential in complex terrains using the above mentioned mean-flow modelling methodology for different surface topographies. Millward-Hopkins *et al.* [7,8] developed a semi-empirical methodology for predicting above-roof mean wind speeds in urban areas and used this information to assess the wind resource potential within cities. They found that there are viable sites scattered throughout a city, including within the complex city centre, where the above-roof wind speeds at the most suitable locations may be comparable to those observed at well-exposed rural sites. Alternately, Vanderwende & Lundquist [9] used different values of roughness lengths from Wieringa [10,11] to assess the impact of crop height at wind farm sites.

In this study, we utilise the data obtained in previous wind-tunnel experiments [1,2] to examine the influence of heterogeneous surface terrain on wind resource. We also briefly consider the fatigue/survivability of wind turbines and farms through an examination of the turbulent stresses. We consider two different types of surface heterogeneities. First, repeated units of roughness topography, where the reference area of the repeated unit scales with the boundary layer thickness, are examined. Within a repeated unit, the frontal solidity (total projected frontal area of roughness per unit wall-parallel area, λ_F) and plan solidity (plan area of roughness per unit wall-parallel area, λ_P) of the surface roughness were varied systematically. Second, the flow features generated by streamwise-aligned strips of LEGO bricks that mimic adjacent

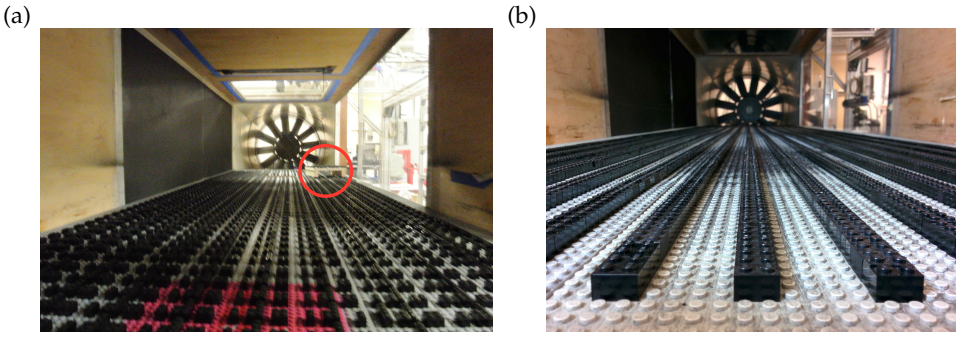

Figure 1. Photographs of the different surface roughness patterns formed with construction bricks. Examples of (a) surfaces with repeating roughness units and (b) surfaces with streamwise-aligned elevated strips. The drag balance patch is also visible to highlight its size (see red circle in (a)).

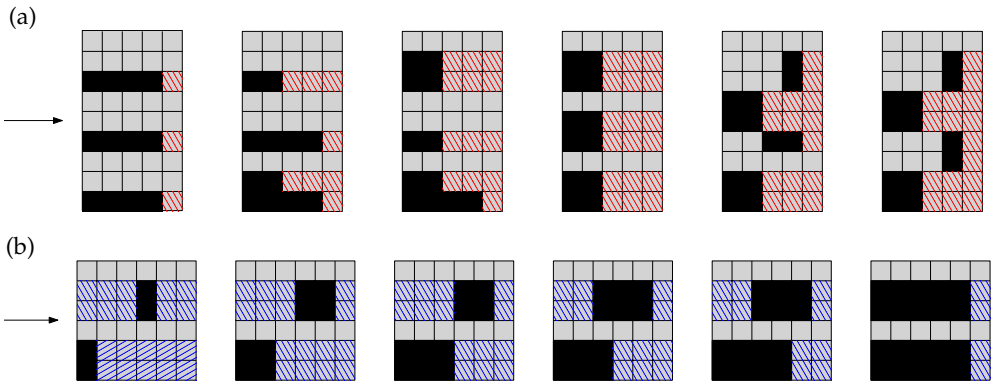

Figure 2. Plan view of the repeated unit of surface roughness patterns that lead to variations in (a) frontal solidity and in (b) plan solidity. The values of the respective solidities increase from left to right (i.e. cases 1 to 6) and the numerical values of the solidities are given in table 1. The flow is left to right. Red and blue shaded areas highlight the streamwise spacing in between roughness repeated units.

hills & valleys (or streets and buildings) were examined. The spacing between adjacent strips of roughness was varied systematically from very fine to really coarse (compared with the boundary layer thickness).

2. Experimental methods

In order to measure the effects of the surface terrain on the flow structure, experiments were performed in the University of Southampton's 3'x2' wind tunnel. The wind tunnel has a test section measuring 0.9 m x 0.6 m x 4.5 m and has nominally zero pressure gradient [12].

In order to create different surface topographies, the floor of the test section was covered with LEGO baseboards, and by using LEGO bricks, we could design a variety of different surface patterns. The LEGO baseboard allows arrangement of the bricks on a regular grid with 8 mm spacing. Examples of different rough surfaces examined herein are shown in figure 1. The LEGO bricks themselves have a nominal height of $H = 9.6$ mm, not including the connecting pins which have a height of 1.8 mm.

As mentioned previously, two different types surface morphologies were examined. First, rough surfaces that contain repeated units of specific surface morphology were generated by distributing the LEGO bricks in different patterns. The main distinguishing feature of all these surface patterns is that the size of the repeated unit is comparable to the thickness of the boundary layer and therefore represents a heterogeneous surface. In most previous studies that use regular roughness elements, the repeated unit was much smaller than the boundary layer thickness. The repeated units were characterised using two solidity parameters: frontal solidity, λ_F, and plan solidity, λ_P. Another distinguishing feature of this study relative to others is that different surfaces with different λ_F are generated at a fixed λ_P and *vice-versa*. A total of 12 surfaces were generated and are shown in figure 2. The top row shows the variation in frontal solidity at a fixed plan solidity while the bottom row shows the variations in plan solidity (at fixed λ_F). Results obtained from these measurements are discussed in section 3.

Second, the LEGO bricks were arranged such that they were aligned along the streamwise direction and the spacing between adjacent rows of aligned and elevated bricks was varied systematically. A total of 5 different surfaces were tested and the spacing between adjacent rows was varied from 0.3δ to 1.8δ, where δ is the local boundary layer thickness. Results from these measurements are presented in section 4.

Measurements of the flow field that developed over the surface were acquired using both planar and stereoscopic Particle Image Velocimetry (PIV). The flow was seeded with vaporised glycol-water solution particles, which were illuminated by a pulsed Nd:YAG laser (200 mJ per pulse). The measurement plane captured a cross-section of the flow located 4 m downstream from the start of the roughness, where the flow has developed over 20δ to ensure the fully-developed conditions [12]. For stereo PIV measurements, particle images were acquired using two cameras positioned on either side of the test section and fitted with Scheimpflug adapters to accommodate the oblique viewing angles. In all cases, 1500 independent image pairs were acquired and converted into vector fields using *LaVision's DaVis* software. Further details are provided in previous articles [1,2].

For the first dataset, the drag generated by the different wall morphologies was directly measured via a floating element drag balance, which was based on the design of [13]. This balance was placed at the same location of the PIV measurements (approximately 4 m downstream along the test section). The reader is referred to [13] and [14] for full details on the balance measurement principle and to [15] for its *in-situ* validation. Once the U_τ was measured, a least-square-fit procedure was used to evaluate the zero-plane displacement, d, and the roughness length, y_0. Since a value of $d > H$ would be physically meaningless in accordance with [6], we forced the condition $d \leq H$, as in [16]. A log-layer region was assumed for $1.5H \leq y \leq 0.2\delta$ as in [17]. The fitting procedure was carried out with a fixed $\kappa = 0.38$. Further details and uncertainty inherent within this method are discussed in [15] and [1].

In this article, the x, y, and z coordinates correspond to the streamwise, vertical, and spanwise directions, respectively. The velocities in the (x, y, z) directions are denoted by (U, V, W). The mean quantities are represented using an overline and the fluctuations in a given direction are denoted by lower case letters.

3. Effect of roughness solidity

In this section, we re-examine the data from [1] to determine the influence of variation in large-scale roughness morphology on wind resource availability.

As previously introduced, the roughness morphology is herewith described via the means of frontal and plan solidities [18]. Based on these two parameters, various morphometric models have been developed to *a-priori* predict the drag generated by a geometrically known surface [19–22]. However, an elegant and universal solution is yet to be found [23]. Most of these morphometric methods follow a semi-empirical approach and they have been historically based on cube roughnesses. These include both numerical and physical experiments [24–30]. It is important to note, however, that cube roughness is not a good benchmark case as, by definition,

$\lambda_F \equiv \lambda_P$. This means that these two solidities are coupled and effects of one or the other cannot be determined independently. To overcome this issue and provide a data set that could be used in developing future morphometric methods, a series of experiments were carried out by systematically varying λ_F at a fixed λ_P and *vice versa*. A total of twelve different configurations (from sparse to dense regimes - cases 1 to 6) were tested with the aim of examining the effect of (non-cubical) surface morphology upon flow characteristics. Some results from this study follow.

(a) The mean flow

Mean streamwise velocity profiles for flow over different rough surfaces are shown in figure 3. The profiles are non-dimensionalised by the values of U_τ (as measured from the drag balance) and y_0 (as determined from the non-linear fit). Although measurements were taken for all twelve surfaces, mean velocity profiles for only three surfaces are shown: the sparse, medium and dense values of λ_F and λ_P, respectively. It should be noted that a thorough description of the flow field and its implication have previously been presented in [1], here we recap some of the main findings in order to set the stage for the subsequent analysis.

For all cases in figure 3, a linear region is clearly visible in the profiles, which offers strong support for the existence of a well defined log-layer. In this region, the good collapse of the roughness data onto the smooth-wall linear asymptote (when scaled with y_0) shows that the roughness length was appropriately evaluated. The figure also seems to show that the logarithmic region extends well into the roughness sublayer in accordance with previous findings [24] and that there is reasonable collapse of the data across the different surface morphologies indicating that the variations in surface roughness do not change the form of the mean wind speed. The roughness, however, alters the drag and hence the values of y_0. It should be noted that the uncertainty in determining a log-region has been significantly reduced herewith (when compared to other rough-wall studies) through the measurement of U_τ using the drag balance. A thorough uncertainty analysis of this balance is here omitted for the sake of brevity, however, it is discussed in [15] to be below 5%. This opposed to the modified Clauser's chart and the total stress methods accuracy, which is much higher (typically of the order of 7% and 10% respectively [17]). Furthermore, it must be noted that the balance results fall within 5% of the values estimated using these commonly used methods.

Also noticeable from the data is a substantial variation in zero-plane displacement, d, for the different surfaces. Table 1 shows the different values of y_0 and d for the various rough surfaces examined in this study, while the reader is referred to [1] for further details on the evaluation of the aerodynamic parameters. It must be noted, when consulting table 1, that the height of the roughness is fixed for all surfaces at $H = 11.4$ mm (which includes the connecting pins on the top of the LEGO bricks).

(b) Wind resource availability

The differences in y_0 and d for different surface morphologies have ramifications for estimating the wind power output. The fact that y_0 changes dramatically with the local terrain means that the shape of the velocity profile also changes, which affects the equivalent wind velocity experienced by a wind turbine. This is defined as [31],

$$U_{eq} \approx \left(\sum_{i=1}^{N} U_i^3 \frac{A_i}{A} \right)^{\frac{1}{3}}, \tag{3.1}$$

where N is the number of discretised levels within the rotor layer, U_i and A_i are the wind speed and fractional area for the i^{th} level, respectively, and A is the total area of the rotor-disk. Each fractional area is assumed to be the sector of the rotor-disk circle bounded by the midpoints between the levels above and below the i^{th} level, as shown in the figure 4a. The magnitude of the differences in U_{eq} that would be experienced by a typical turbine placed at different points

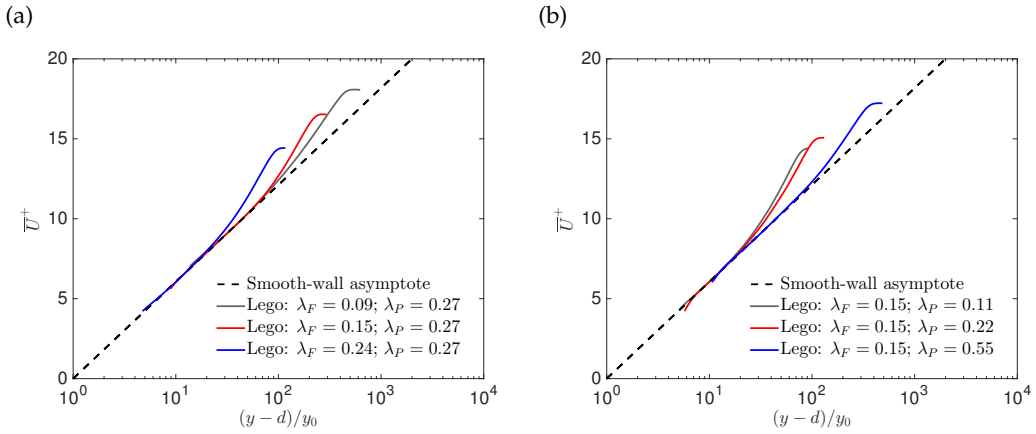

Figure 3. Mean velocity profiles in y_0 scaling of flow over surfaces with variations in (a) λ_F and (b) λ_P.

Case ID	λ_F	λ_P	H/δ	$U_\tau(m/s)$	d/H	y_0/H
LF1	0.09	0.27	0.10	0.65	0.98	0.02
LF2	0.12	0.27	0.09	0.73	0.59	0.05
LF3	0.15	0.27	0.09	0.71	0.80	0.04
LF4	0.18	0.27	0.09	0.80	0.74	0.10
LF5	0.21	0.27	0.09	0.82	0.61	0.12
LF6	0.24	0.27	0.09	0.81	0.73	0.11
LP1	0.15	0.11	0.08	0.81	0.50	0.14
LP2	0.15	0.22	0.09	0.78	0.68	0.10
LP3	0.15	0.27	0.09	0.71	1.00	0.05
LP4	0.15	0.33	0.09	0.67	0.92	0.05
LP5	0.15	0.39	0.10	0.66	0.97	0.04
LP6	0.15	0.55	0.10	0.67	0.97	0.03

Table 1. Relevant experimental parameters for frontal (LF1 to LF6) and plan (LP1 to LP6) solidity cases. The aerodynamic parameters are calculated through a log-law fit with $\kappa = 0.38$ in the range $1.5H \leq y \leq 0.2\delta$.

in the terrain can be estimated by using the values of y_0/h_f and d/h_f in table 1 (where h_f is the representative height of the surface; in these experiments, this was taken to be the total height of the LEGO brick, $H = 11.4\ mm$). The logarithmic profile can be used to predict the variation of the wind speed across the rotor diameter. For example, assuming a typical turbine, 67 m tall with a hub diameter of 80 m, placed in a boundary layer with a thickness of 750 m over the terrain, the equivalent wind speed can be calculated for different rough surfaces. Assuming a feature height h_f = 5m, for an arbitrary reference speed of U_{ref} of 4 m/s at a height of 10 m above the local surface, which is in the logarithmic region of the flow, the velocity profile across the rotor can be constructed for given values of y_0 and d, as shown in figure 4b.

Figure 5 shows the equivalent wind speed for different values of λ_F and λ_P normalised by the reference velocity U_{ref}. These values were obtained by generating mean wind speed profiles for different values of y_0 and d and using them to determine the equivalent wind speed. The figure clearly shows the dependence of power extraction potential on the surface morphology. Increasing values of λ_F results in increasing values of U_{eq} indicating that a higher drag coefficient essentially means a higher momentum flux across the rotor diameter and therefore a larger amount of energy that can be extracted from the wind. Similarly, increasing λ_P results in a decreasing trend in U_{eq}, where progressive shielding of downstream roughness elements by the

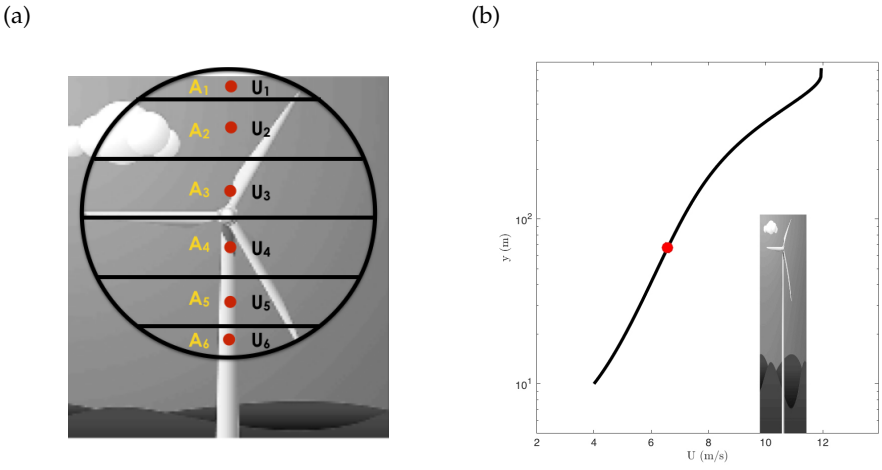

Figure 4. (a) Schematic to represent the calculation of the equivalent rotor wind speed, (b) mean wind profile computed using the values of y_0 and d for a given rough surface assuming a reference speed of 4 m/s at a height of 10m above ground. The red dot marks the hub velocity (at the hub height) in the profile.

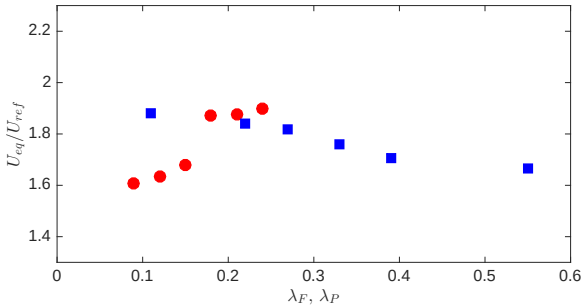

Figure 5. Equivalent wind speed (U_{eq}) normalised by reference wind speed (U_{ref}) of 4 m/s at a height of 10m above ground. The red circles is for variation in λ_F and the blue squares are for variations in λ_P.

upstream elements leads to decreased momentum flux from the surface. This is reflected in the reduced power potential across the rotor diameter. Overall, the equivalent wind speed appears to have a variation of approximately 20% across the different surface morphologies. It should be noted that variations in plan solidity at a fixed frontal solidity were achieved by placing more roughness elements in the wake of upstream ones. This resulted in a sheltering effect whereby the flow would transition from a separating/reattaching flow to a skimming flow. At the highest value of λ_P (bottom right in figure 2b), the surfaces appear to resemble parallel hills and valleys, albeit there is a small gap along the hills, as highlighted by the blue-shaded area.

The above analysis required us to make assumption about turbine hub height, diameter and boundary layer thickness (in addition to empirical laws such as logarithmic region and roughness lengths). A more general trend that does not requires these assumptions can be derived by examining the measured profiles of mean-squared and mean-cubed values of streamwise velocities ($\overline{U^2(y)}$ and $\overline{U^3(y)}$, respectively). These quantities are proportional to the thrust and power that can be extracted from the wind at a given height. Figure 6a&b show the mean-squared velocity profiles, for the same frontal and plan solidity cases in figure 3, on the left and right respectively. The variance of this quantity at the same wall-normal locations are also shown (dashed lines). It is clear how, for both cases, the unsteadiness in the winds (i.e. the variance

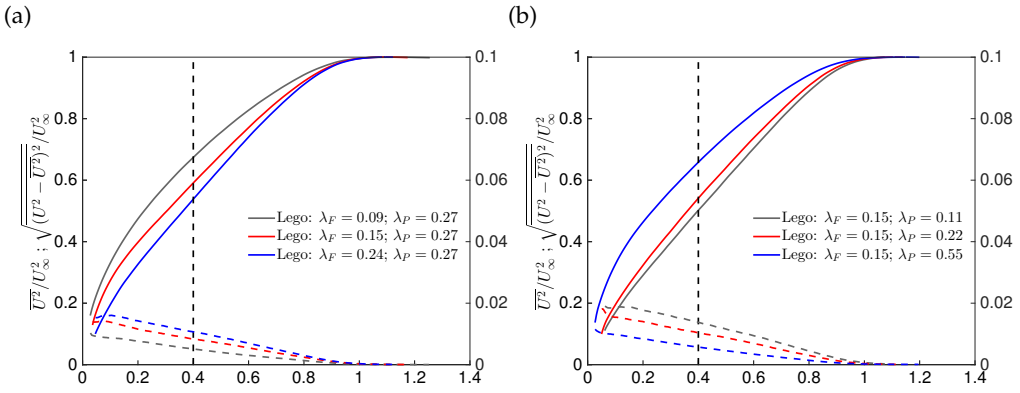

Figure 6. Mean squared velocity (solid lines) and its standard deviation (dashed lines) for (a) λ_F and (b) λ_P. Black dashed lines run along a fixed height location.

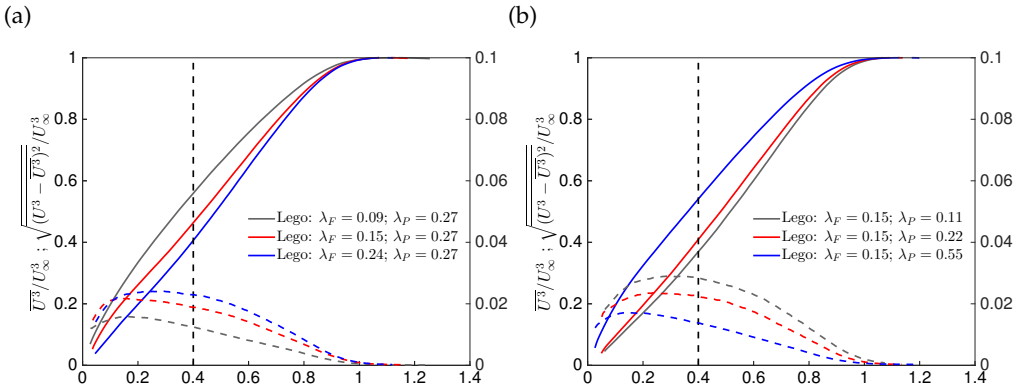

Figure 7. Mean cubed velocity (solid lines) and its standard deviation (dashed lines) for (a) λ_F and (b) λ_P. Black dashed lines run along a fixed height location.

of U^2) increases going towards the edge of the roughness sublayer, where the flow is bound to have more spanwise variation. At a fixed wall-normal location, e.g. $(y-d)/\delta \approx 0.4$ (as marked by the black dashed line), the variation in the velocity squared profile for the frontal solidity cases in between the grey and the blue curves (from a sparse to a dense regime) is of the order of 20%. At the same height, the variation across the plan solidity cases, as shown in figure 6b, is instead approximately 25%. The trends are also opposite in the two cases as sparser λ_F regimes generally are characterised by higher available thrust across the entire height (see grey line), while the opposite is true for variation in λ_P. This suggests that regardless of the wind turbine height and diameter, the thrust produced for sparse λ_F (at a given λ_P) and dense λ_P (at a given λ_F) would be the highest.

The cubed velocity profiles are proportional to the power of the available wind energy, which is consistent with the calculation of the equivalent wind speed presented earlier. These trends are presented in figure 7a&b, and exhibit a similar behaviour to that exhibited by thrust for both λ_F and λ_P cases. At the same fixed height of $(y-d)/\delta \approx 0.4$, the variation of available power across the frontal solidity cases is approximately 29% against a range of up to 35% across the plan solidity cases. It is also clear by comparing the dashed lines in figures 6 and 7 that the variance of U^3 is much larger than the same quantity for U^2, which indicates a lower variability of the thrust

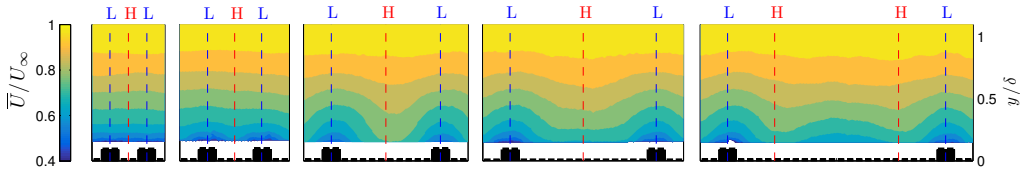

Figure 8. Maps of the mean velocity in cross-sections of the flow illustrate the presence of the secondary flows that form over five different cases of streamwise-aligned roughness (with centre-to-centre spacings of S/δ =0.29, 0.44, 0.89, 1.16 and 1.74). Dashed blue and red lines indicate the locations of the low-momentum pathways located atop peaks in the surface and the high-momentum pathways in the valleys, respectively.

output as opposed to the power. It should be noted that, all other cases in table 1 lie between the grey and blue lines in figures 6 and 7, and therefore are omitted for clarity. It should also be pointed out that these curves are only valid for a constant thrust and power coefficients (often referred to in the literature as C_T and C_P respectively) and therefore for a fixed blade geometry.

4. Spanwise heterogeneity in surface terrain

Terrain with heterogeneities along the spanwise direction has been shown to generate secondary flows that manifest as large counter-rotating vortices with axes aligned in the streamwise direction [32,33]. These secondary flows create low- and high- momentum pathways that impact the entire boundary layer thickness and can have serious implications for wind resources as they result in inhomogeneities in the mean wind velocity and turbulence properties. In order to determine the appropriate length scale of the spanwise heterogeneity that will generate the secondary flows, we tested different cases with surface features that were aligned in the streamwise direction (see figure 1b).

(a) The mean flow

The time-averaged flow fields resulting from these roughness distributions have previously been presented [2] and are summarised in figure 8 in order to set the stage for the subsequent analysis. We found that the secondary flows were most accentuated when the spacing of the elevated surface features was roughly equal to the boundary layer thickness. For finer spacing, the secondary flows were confined to the roughness sublayer (20-30% of δ). For coarser spacings, the secondary flows still existed but were weakened with respect to the optimal case and were capable of creating tertiary vortex pairs at harmonics of the surface spacing.

When present, the secondary flows resulted in low-momentum pathways (LMPs) aligned with the elevated surfaces and high-momentum pathways (HMPs) in the valleys in between. For all the cases we considered, the HMP was located in the centre of the valley, with the exception of the coarsest spacing where HMPs were located offset from the centre, due to the presence of tertiary vortices in the valley. The variation of the streamwise velocity in these LMPs and HMPs could differ by as much as 20% from the spanwise-averaged mean velocity.

The variation of the in-plane velocities of the counter-rotating vortices was not nearly as severe, having magnitudes of approximately 2% of U_∞. This value is in fact comparable to the turbulence intensity, u'/U_∞, which ranged from 1.5% in the free stream to 10% at the wall. This means that, while the secondary flows dramatically alter the streamwise velocity magnitude, they would not severely impact the mean flow angle.

The generation of secondary flows have serious ramifications for flows over arbitrary surfaces as even apparently random surfaces can develop secondary flows [33]. We suggest that the necessary condition for secondary flows to exist is that the surface exhibits any sort of periodicity in the direction perpendicular to the flow that has a scale on the order of the boundary layer

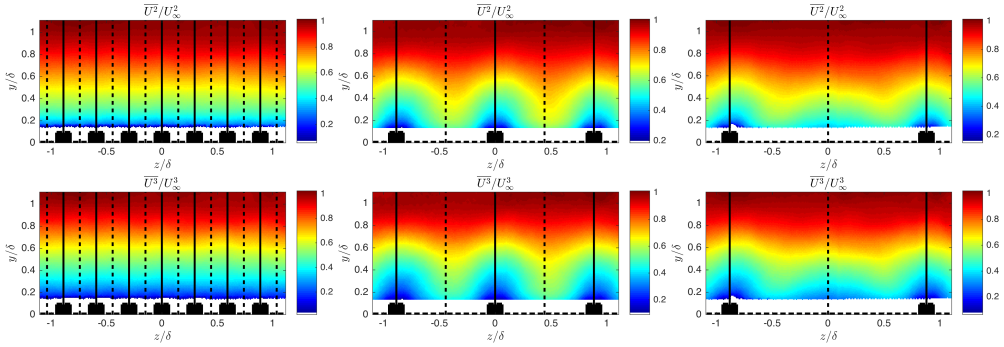

Figure 9. Maps of the $\overline{U^2}$ and $\overline{U^3}$ over three different cases of streamwise-aligned roughness (with centre-to-centre spacings of S/δ =0.29, 0.89 and 1.74). Dashed and solid black lines indicate the locations of the low- and high-momentum pathways located atop of peaks and valleys, respectively.

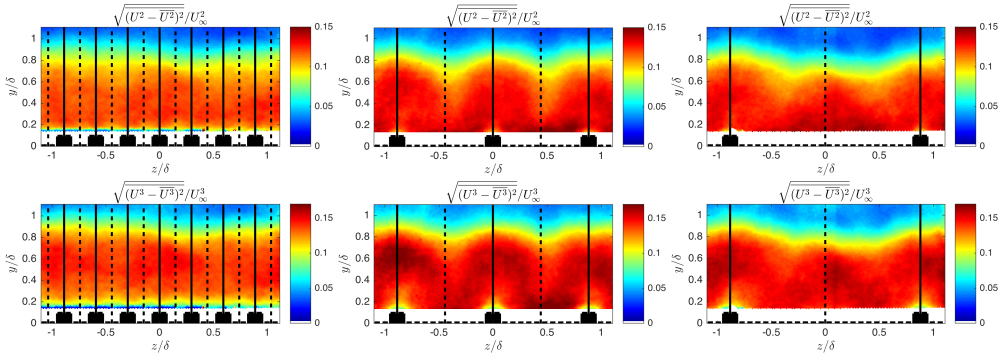

Figure 10. Maps of the standard deviations of U^2 and U^3 over three different cases of streamwise-aligned roughness (with centre-to-centre spacings of S/δ =0.29, 0.89 and 1.74). Dashed and solid black lines indicate the locations of the low- and high-momentum pathways located atop of peaks and valleys, respectively.

thickness [2]. Therefore, in atmospheric flows where $\delta \sim 1$km, we would expect secondary flows to manifest in the presence of any km-scale variations in the surface terrain, which could include natural, agricultural, or urban variations in terrain.

(b) Thrust and power in the presence of secondary flows

As in the previous section, the thrust and power potential of wind flows over these heterogeneous terrains can be derived from contours of $\overline{U^2}$ and $\overline{U^3}$ across the flow. Figure 9 shows contours of both quantities for three different surface terrains (different spacings between streamwise-aligned roughness). It can be clearly seen, just as in the previous case, that different terrain exhibit different thrust and power potential. There is a remarkable difference between the hills and valleys even within the cases examined here (three out of the five presented in figure 8). For low spacing between hills (S/δ = 0.29), the variation in thrust and power appears to be negligible. As the spacing is increased to S/δ = 0.89, the variation in thrust and power potential becomes significant and follows (in fact, accentuates) the secondary flow arrangement found in the mean flow. For even higher spacing (S/δ = 1.74), the variation between hill and valley is reduced, due to the presence of tertiary flows. For example, at a height of 0.2δ above the surface (assuming a turbine with hub-height at this location), the differences in thrust and power between peak and valley are negligible for S/δ = 0.3. At the same height, these differences increase to over 60% for S/δ = 0.89.

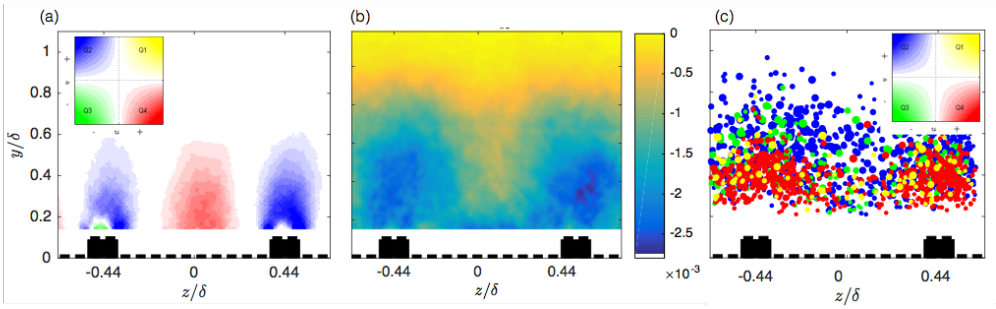

Figure 11. (a) Dispersive Reynolds shear stress (normalised by U_∞^2) for S/δ = 0.89. Red contours show sweep events and blue contours show ejections. The contour levels for blue and red contours are identical and range from 0 to -0.8U_∞^2 in 10 levels. (b) Turbulent shear stress ($\overline{-u'v'}/U_\infty^2$) for S/δ = 0.89, which shows effect of secondary flows persist beyond the dispersive stresses. (c) Distribution of turbulent shear stress events across the boundary layer for S/δ = 0.89. The figure shows turbulent shear stress activity (both sweeps and ejections) is concentrated above the hills. The colour indicates the quadrant and the size indicates the strength of the events.

For the highest spacing case, the differences are reduced to just around 30%. However, for this spacing, if a spanwise location that is at the mid-point between the hill and valley is chosen, then the differences are back up to nearly 60%. These differences are consistent over a range of wall-normal locations within the boundary layer. Therefore, it can be concluded that these differences in thrust and power can be expected regardless of the hub-height and rotor diameter.

Figure 10 shows the variance in U^2 and U^3, which gives an indication of the variance in thrust and power output for these different heterogeneous terrains. For S/δ = 0.29, the variation in the variance is not significant, as a uniform variance is found across the terrain. As the spacing increases to S/δ = 0.89, the variance in thrust exhibits similar characteristics to the behaviour of the squared velocity with an overall variance that increases marginally. For power, the variation in variance between the hill and the valley appears to be more significant. For example, at the same height (y/δ = 0.2), the difference in thrust appear to be around 15% but for power the differences are much higher (nearly 50%). Finally, for S/δ = 1.74, the variation in variance between hill and valley increases further. It is important to note that the variance in thrust and power is much higher farther away from the surface. Therefore, larger hub-heights and rotor diameters will be impacted significantly in the presence of secondary flows.

(c) Dispersive and turbulent stresses

It is clear that secondary flows can significantly affect the local velocity, thrust and power profiles, but it is also important to be aware of the local Reynolds shear stresses (which describe the correlations between turbulent fluctuations) and how they may also vary with respect to the local topography. Figure 11 shows maps of dispersive shear stress (i.e. spatially varying, $\tilde{u}\tilde{v}$) and Reynolds shear stress (time-varying, $\overline{uv}$) for flow over streamwise-aligned roughness with S/δ = 0.89. It can be clearly seen from the dispersive stresses (in figure 11a) that "sweeps" ($u' > 0, v' < 0$) are dominant in the valleys while "ejections" ($u'<0, v'>0$) are significant in the peaks. These dispersive stresses are present across the entire height of the boundary layer and are a manifestation of the secondary flows introduced by the heterogeneous terrain.

Figure 11b also shows that the turbulent shear stress exhibit strong activity over the hills and this activity reduces in strength in the valleys. This suggests that the shear stress fluctuations are higher over the hills, which is a higher order effect of the secondary flows. Therefore, for this spacing (S/δ = 0.89), the presence of secondary flows essentially result in stronger turbulent activity in the regions above the hills and an attenuation of turbulent activity in the valleys. This is further highlighted by examining the distribution of quadrant events that is responsible for

the turbulent shear stresses. Figure 11c shows the distribution of quadrant events (in coloured circles) of varying strengths (size of the circles). This figure clearly shows that both the strength of the activity as well as the population of the activity is higher over the hills compared to the valleys. Both sweeps and ejections are strong over the hills. This suggests that the flow is "more" turbulent over the hills. Therefore, turbines placed on top of these streamwise-aligned hills could encountered higher fluctuations both as far as the instantaneous flow angles and the turbulent shear stresses. This could have a critical impact on overall power output as well as fatigue life of these turbines.

5. Conclusions

In this study, data obtained in previous experiments were re-analysed to examine the influence of heterogeneous surface morphology on wind resource potential. Two different types of surface heterogeneities were examined. First, surfaces with repeating roughness units on the order of the boundary layer thickness were examined. These surfaces were parametrised using frontal and plan solidities and the influence of variation of each parameter (with the other fixed) was studied. The wind resource potential of different surface morphologies shows that the power extraction potential is highly dependent on the surface morphology with a variation of about 20% across the different surfaces examined herewith. A strong correlation is shown to exist between the frontal and plan solidities of the rough surfaces and the equivalent wind speed, as well as the local power and thrust factors. Second, surfaces with streamwise-aligned elevated strips that mimic adjacent hills were considered. For this second case, measurements suggest that the streamwise strips of roughness generate secondary flows that manifest themselves as low- and high-momentum pathways. These secondary structures (that are statistically stationary) are most accentuated when the spanwise spacing of the roughness elements was roughly proportional to the boundary layer thickness. Under these circumstances, there is wide range of variation in wind resource availability across the different cases. Differences in power and thrust of up to 60% can be seen for a fixed height above ground, depending on the spanwise location. Regions above the hills have generally a lower thrust/power potential compared to regions in the valleys, however, the variance of thrust and power is also an important parameter to consider. The latter is larger in valleys compared to hills. Finally, shear stress distribution (both dispersive as well as turbulent components) across the heterogeneous terrain is found to be significantly different, which could lead to variable fatigue life depending on the placement of the turbines.

Authors' Contributions. BG conceived the research programme. CV and MP carried out the experiments. BG, CV and MP performed the data analysis and contributed to drafting the manuscript. All authors read and approved the manuscript.

Competing Interests. The authors declare that they have no competing interests.

Funding. We gratefully acknowledge the financial support from the European Research Council (ERC grant agreement no. 277472), EPSRC (grant ref no: EP/I037717/1) and the European Commission (project ref no. 656081).

Acknowledgements. We thank our friends and colleagues who helped assemble all the LEGO bricks in the wind tunnel. We thank two anonymous referees and the editors of this special issue for their suggestions that enabled us to improve the quality of this manuscript.

References

1. Placidi M, Ganapathisubramani B. 2015 Effects of frontal and plan solidities on aerodynamic parameters and the roughness sublayer in turbulent boundary layers. *Journal of Fluid Mechanics* **782**, 541–566.
2. Vanderwel C, Ganapathisubramani B. 2015 Effects of spanwise spacing on large-scale secondary flows in rough-wall turbulent boundary layers. *Journal of Fluid Mechanics* **774**, 1–12.
3. Bottema M. 1996 Urban roughness modelling in relation to pollutant dispersion.

Journal of Wind Engineering and Industrial Aerodynamics **31**, 3059–3075.
4. Millward-Hopkins J, Tomlin A, Ma L, Ingham D, Pourkashanian M. 2012 Aerodynamic Parameters of a UK City Derived from Morphological Data.
Boundary-Layer Meteorology **146**, 447–468.
5. Crago R, Okello W, Jasinski M. 2012 Equations for the Drag Force and Aerodynamic Roughness Length of Urban Areas with Random Building Heights.
Boundary-Layer Meteorology **145**, 423–437.
6. Jackson P. 1981 On the displacement height in the logarithmic velocity profile.
Journal of Fluid Mechanics **111**, 15–25.
7. Millward-Hopkins J, Tomlin A, Ma L, Ingham D, Pourkashanian M. 2012 The predictability of above roof wind resource in the urban roughness sublayer.
Wind Energy **15**, 225–243.
8. Millward-Hopkins J, Tomlin A, Ma L, Ingham D, Pourkashanian M. 2013 Assessing the potential of urban wind energy in a major uk city using an analytical model.
Renewable energy **60**, 701–710.
9. Vanderwende B, Lundquist JK. 2016 Could crop height affect the wind resource at agriculturally productive wind farm sites?
Boundary-Layer Meteorology **158**, 409–428.
10. Wieringa J. 1992 Updating the davenport roughness classification.
Journal of Wind Engineering and Industrial Aerodynamics **41**, 357–368.
11. Wieringa J. 1993 Representative roughness parameters for homogeneous terrain.
Boundary layer Meteorology **63**, 323–363.
12. Castro IP. 2007 Rough-wall boundary layers: mean flow universality.
J. Fluid Mech. **585**, 469–485.
13. Krogstad PÅ, Efros V. 2010 Rough wall skin friction measurements using a high resolution surface balance.
International Journal of Heat and Fluid Flow **31**, 429–433.
14. Efros V. 2011 *Scructure of turbulent boundary layer over a 2-D roughness*.
Ph.D. thesis, Norwegian University of Science and Technology.
15. Placidi M. 2015 *On the effect of surface morphology on wall turbulence*.
Ph.D. thesis, University of Southampton. Engineering and the Environment.
16. Iyengar AKS, Farell C. 2001 Experimental issues in atmospheric boundary layer simulations: roughness length and integral length scale determination.
Journal of Wind Engineering and Industrial Aerodynamics **89**, 1059–1080.
17. Schultz MP, Flack KA. 2005 Outer layer similarity in fully rough turbulent boundary layers.
Experiments in Fluids **38**, 328–340.
18. Schlichting H. 1937 Experimental investigation of the problem of surface roughness.
NACA TM **823**, 1–60.
19. Moody LF. 1944 Friction factors for pipe flow.
Trans. ASME **66**, 671–684.
20. Macdonald RW. 1998 An improved method for the estimation of surface roughness of obstacle arrays.
Boundary-Layer Meteorology **97**, 1857–1864.
21. Grimmond CSB, Oke TR. 1999 Aerodynamic properties of urban areas derived from analysis of surface form.
J. Appl. Meteorol. **38**, 1262–1292.
22. Millward-Hopkins J, Tomlin A, Ma L, Ingham D, Pourkashanian M. 2011 Estimating aerodynamic parameters of urban-like surfaces with heterogeneous building heights.
Boundary-layer meteorology **141**, 443–465.
23. Yang XI, Sadique J, Mittal R, Meneveau C. 2016 Exponential roughness layer and analytical model for turbulent boundary layer flow over rectangular-prism roughness elements.
Journal of Fluid Mechanics **789**, 127–165.
24. Cheng H, Castro IP. 2002 Near wall flow over urban-like roughness.
Boundary-Layer Meteorology **105**, 411–432.
25. Coceal O, Belcher S. 2004 A canopy model of mean winds through urban areas.
Quarterly Journal of the Royal Meteorological Society **130**, 1349–1372.
26. Kanda M, Moriwaki R, Kasamatsu F. 2004 Large-eddy simulation of turbulent organized structures within and above explicitly resolved cube arrays.
Boundary-Layer Meteorology **112**, 343–368.

27. Cheng H, Hayden P, Robins A, Castro I. 2007 Flow over cube arrays of different packing densities.
Journal of Wind Engineering and Industrial Aerodynamics **95**, 715–740.
28. Santiago J, Coceal O, Martilli A, Belcher S. 2008 Variation of the sectional drag coefficient of a group of buildings with packing density.
Boundary-layer meteorology **128**, 445–457.
29. Hagishima A, Tanimoto J, Nagayama K, Meno S. 2009 Aerodynamic parameters of regular arrays of rectangular blocks with various geometries.
Boundary-Layer Meteorology **132**, 315–337.
30. Leonardi S, Castro IP. 2010 Channel flow over large cube roughness: a direct numerical simulation study.
Journal of Fluid Mechanics **651**, 519–539.
31. Wagner R, Antoniou I, Pedersen SM, Courtney MS, Jørgensen HE. 2009 The influence of the wind speed profile on wind turbine performance measurements.
Wind Energy **12**, 348–362.
32. Barros JM, Christensen KT. 2014 Observations of turbulent secondary flows in a rough-wall boundary layer.
Journal of Fluid Mechanics **748**, R1.
33. Anderson W, Barros JM, Christensen KT, Awasthi A. 2015 Numerical and experimental study of mechanisms responsible for turbulent secondary flows in boundary layer flows over spanwise heterogeneous roughness.
Journal of Fluid Mechanics **768**, 316–347.